Article

Comparative Study of Preparation and Electrochemical Properties of $Nb_4C_3T_x$ (T = –OH, –F, or =O) and $(Nb_{0.8}Ti_{0.05}V_{0.05}Zr_{0.05}Ta_{0.05})_4C_3T_x$ (T = –OH, –F, or =O) MXenes

Ming Fu [1], Hongyu Chen [2,*], Juan Cheng [2], Longsheng Chu [2], Qingguo Feng [2] and Chunfeng Hu [2,*]

[1] Nuclear Power Institute of China, Chengdu 610213, China; fm7887077@163.com

[2] Key Laboratory of Advanced Technologies of Materials, Ministry of Education, School of Materials Science and Engineering, Southwest Jiaotong University, Chengdu 610031, China; 17782174450@163.com (J.C.); lshchu@swjtu.edu.cn (L.C.); qfeng@swjtu.edu.cn (Q.F.)

* Correspondence: hychen_1999@163.com (H.C.); chfhu@live.cn (C.H.)

Abstract: Two–dimensional MXene synthesized from MAX phase ceramic has good electrical conductivity, promising to be used as electrodes. In this study, $Nb_4C_3T_x$ (T = –OH, –F, or =O) MXene and low–entropy $(Nb_{0.8}Ti_{0.05}V_{0.05}Zr_{0.05}Ta_{0.05})_4C_3T_x$ (T = –OH, –F, or =O) MXene were prepared by etching Nb_4AlC_3 and $(Nb_{0.8}Ti_{0.05}V_{0.05}Zr_{0.05}Ta_{0.05})_4AlC_3$ ceramics in the HF acid at 60 °C. By investigating the electrochemical properties of lithium batteries, it was found that the $Nb_4C_3T_x$ and $(Nb_{0.8}Ti_{0.05}V_{0.05}Zr_{0.05}Ta_{0.05})_4C_3T_x$ could provide the specific capacities of 163.7 mAh·g^{-1} and 130 mAh·g^{-1} after 50 cycles at a current density of 0.1 A·g^{-1}, respectively, and maintain the coulombic efficiency close to 100%, good for the utilization of electrodes in lithium batteries.

Keywords: Nb_4AlC_3; $(Nb_{0.8}Ti_{0.05}V_{0.05}Zr_{0.05}Ta_{0.05})_4AlC_3$; MXene; lithium battery; electrochemical property

1. Introduction

MXene is a new 2D material, first synthesized by Naguib et al. in 2011 [1]. Here, the name "MXene" comes from the combination of "M" for the transition metal, "X" for carbon or nitrogen, and "ene" to signify the presence of the two–dimensional layers. Typically, MXene is obtained by selective removal of the A–atom layer from the MAX phases which are ternary compounds composed of a transition metal (M), an element from group 13 or 14 (A), and carbon or nitrogen (X) using etchants (HF, LiF, HCl, etc.) [1,2]. It not only has the high specific surface area of 2D materials but also has a high electrical conductivity similar to that of the MAX phase. The etching process enriches the surface of MXene with surface groups, giving it hydrophilic and surface modification potential [3]. The excellent properties of MXene make it promising for a wide range of applications in energy storage [4–7], catalysis [8,9], adsorption [10], hydrogen storage [11], and medicine [12], especially in the field of energy storage.

The high–entropy materials that appeared in 2004 can exhibit excellent performance due to the high–entropy effect [13–15]. Subsequently, the concept of high entropy quickly extended to the study of ceramics [16]. In 2021, Yang et al. first reported high–entropy MXene (HE–MXene) [17]. After that, other researchers followed up the research quickly. Their research focused on the development of nearly equimolar ratios HE–MXene based on Ti–based MXene that were mainly applied to lithium–ion batteries [17,18], Li–S ion batteries [19], and capacitors [20,21], etc. Among them, the HE–MXene reported by Yang et al. as an anode still maintained a capacity of 150 mAh·g^{-1} after 50 cycles at 0.5 C [17]. Rosen et al. reported that the capacity also reached 126 mAh·g^{-1} at a rate of 0.01 C [18]. However, the effect of entropy increase on the energy storage performance of MXene is still not too clear. Therefore, in this work, Nb–based MXene was subjected to entropy increase treatment, and its effect on electrochemical performance was systematically studied.

In this work, low–entropy Nb–based 413 MAX phase (LE–MAX, $(Nb_{0.8}Ti_{0.05}V_{0.05}Zr_{0.05}Ta_{0.05})_4AlC_3$) and Nb_4AlC_3 ceramics were synthesized by spark plasma sintering (SPS). The corresponding low–entropy MXene (LE–MXene) $(Nb_{0.8}Ti_{0.05}V_{0.05}Zr_{0.05}Ta_{0.05})_4C_3T_x$ and $Nb_4C_3T_x$ were then obtained by etching, and their performance as the anode materials for lithium–ion batteries was investigated comparatively. Here, T refers to the groups that enter the MX interlayers during the etching process, such as –OH, –F, or =O.

2. Experimental Procedures

2.1. Synthesis of LE–MAX Phase

Commercial Nb, Ti, V, Zr, Ta, Al, and C powders were mixed and sintered by spark plasma sintering (SPS) to prepare the LE–MAX phase. Specifically, the elemental powders of Nb (99.5%, 400 mesh) (ENO High–tech Materials Development Co., Ltd., Qinhuangdao, China), Ti (99.5%, 500 mesh) (ENO High–tech Materials Development Co., Ltd., China), V (99.5%, 500 mesh) (ENO High–tech Materials Development Co., Ltd., China), Zr (99.5%, 500 mesh) (ENO High–tech Materials Development Co., Ltd., China), Ta (99.5%, 500 mesh) (ENO High–tech Materials Development Co., Ltd., China), Al (99.9%, 500 mesh) (ENO High–tech Materials Development Co., Ltd., China), and C (99.9%, 500 mesh) (ENO High–tech Materials Development Co., Ltd., China) were weighed based on the designed molar ratio of Nb:Ti:V:Zr:Ta:Al:C = 3.2:0.2:0.2:0.2:0.2:1.39:2.67 using an electrical balance (10^{-4} g accuracy) and mixed in an agate jar for 12 h at 50 rpm. After sieving, the mixture was put into a graphite die with a diameter of 20 mm and sintered in a spark plasma sintering furnace (SPS–20T–10, Chenhua Technology Co., Ltd., Shanghai, China). The sample was gradually heated to 1475 °C in argon atmosphere under a pressure of 30 MPa and then was annealed at 1475 °C for 16 min for consolidation. After sintering, the sample was naturally cooled down with the furnace. After that, the sample was taken out of the graphite die, and the surface graphite paper was removed using a diamond grinding wheel. Then, the sample was crushed into powder, and the 400 mesh standard sieve was used for screening to get fine particles. Finally, the 400–mesh LE–MAX $(Nb_{0.8}Ti_{0.05}V_{0.05}Zr_{0.05}Ta_{0.05})_4AlC_3$ powder was successfully obtained. For comparison, Nb_4AlC_3 sample was also prepared using the same procedure by sintering the powder mixture with a molar ratio of Nb:Al:C = 4:1.39:2.67.

2.2. Preparation of LE–MXene

The LE–MAX $(Nb_{0.8}Ti_{0.05}V_{0.05}Zr_{0.05}Ta_{0.05})_4AlC_3$ powder was mixed with 40 wt% HF acid in a ratio of 1 g: 15 mL and kept in an oil bath facility with magnetic stirring for a certain time (12 h, 24 h, 40 h, 48 h, 120 h) at a constant temperature (room temperature (RT), 50 °C, 60 °C). After etching, the etched powder was rinsed with deionized water and separated by centrifugation. The etched sample was repeatedly washed three times until the pH value of the suspension was close to 7 and then was washed twice with pure alcohol. The LE–MXene $(Nb_{0.8}Ti_{0.05}V_{0.05}Zr_{0.05}Ta_{0.05})_4C_3T_x$ sample was then placed in a desiccator and dried at 40 °C for 12 h. Similarly, $Nb_4C_3T_x$ was prepared using the same etching procedure.

2.3. Material Characterization and Electrochemical Performance

The phase compositions of the as–prepared materials were analyzed using an X–ray diffractometer (DX–2700BH, Haoyuan Instrument Co., Ltd., Dandong, China) with Cu Kα radiation (λ = 1.54178 Å). The scanning speed was set to 0.02°/step. The microscopic morphology and elemental distribution of the sample particles were determined using a scanning electron microscope (Apreo 2, Thermo Fisher Scientific, Waltham, MA) equipped with an energy–dispersive spectrometer. The LE–MXene $(Nb_{0.8}Ti_{0.05}V_{0.05}Zr_{0.05}Ta_{0.05})_4C_3T_x$, carbon nanofibers, and polyvinylidene fluoride (PVDF) were mixed according to the weight ratio of 7:2:1, and then 5 mL of N–methyl pyrrolidone (NMP) solution was added. After that, the mixture was mixed by using a planetary ball mill machine at 500 rpm for 12 h. Then, the mixture was uniformly coated on a copper foil using a coating machine and dried to obtain an electrode plate with a thickness of about 50 μm. The performance of LE–MXene

$(Nb_{0.8}Ti_{0.05}V_{0.05}Zr_{0.05}Ta_{0.05})_4C_3T_x$ as electrode material was tested by assembling lithium–ion half–cell (battery specification: CR2032 button battery; counter electrode: lithium sheet; secondary electrolyte: 1.0 M LiPF6 in the solution of ethylene carbonate (EC) and Dimethyl carbonate (DMC) (1:1)). Cyclic voltammetry was tested on an electrochemical workstation (CS350H, Corrtest Instruments Co., Ltd., Wuhan, China) at a scanning rate of 0.1 mV·s^{-1}. The galvanostatic charge–discharge test and rate performance test were conducted on the battery detection system (CT2001A, Wuhan Land Co., Ltd., Wuhan, China). Electrochemical impedance spectra (EIS) were also measured using the electrochemical workstation (100 kHz~0.01 Hz, 10 mV).

3. Results and Discussion

Figure 1 shows the X–ray diffraction (XRD) patterns of Nb–based LE–MAX $(Nb_{0.8}Ti_{0.05}V_{0.05}Zr_{0.05}Ta_{0.05})_4AlC_3$ and Nb_4AlC_3 samples prepared by spark plasma sintering. It is seen that the diffraction peaks of LE–MAX are shifted to higher angles than those of Nb_4AlC_3. For example, the (106) peak is shifted from $2\theta = 40.04°$ to $2\theta = 40.10°$, and the corresponding crystal plane spacing d is reduced from 2.2500 Å to 2.2468 Å. The reason lies in that V (171 pm), Zr (206 pm), Ti (176 pm), and Ta (200 pm) atoms are added to the M–site, and their average atomic radius is smaller than that of Nb (198 pm) [17,20,22,23]. In addition, the synthesized LE–MAX ceramic is relatively pure, whereas there is a small amount of impurity phases Nb_6C_5 and Nb_2AlC existing in the Nb_4AlC_3 sample. Based on the scanning electron microscopy (SEM) image (Figure 2a) and energy–dispersive spectroscopy (EDS) analysis on the polished surface of the LE–MAX sample (Figure 2b–f), it is seen that the M–site elements are evenly distributed in the grains without obvious segregation. Therefore, LE–MAX $(Nb_{0.8}Ti_{0.05}V_{0.05}Zr_{0.05}Ta_{0.05})_4AlC_3$ ceramic is confirmed to be a relatively uniform solid solution, which is consistent with the XRD result.

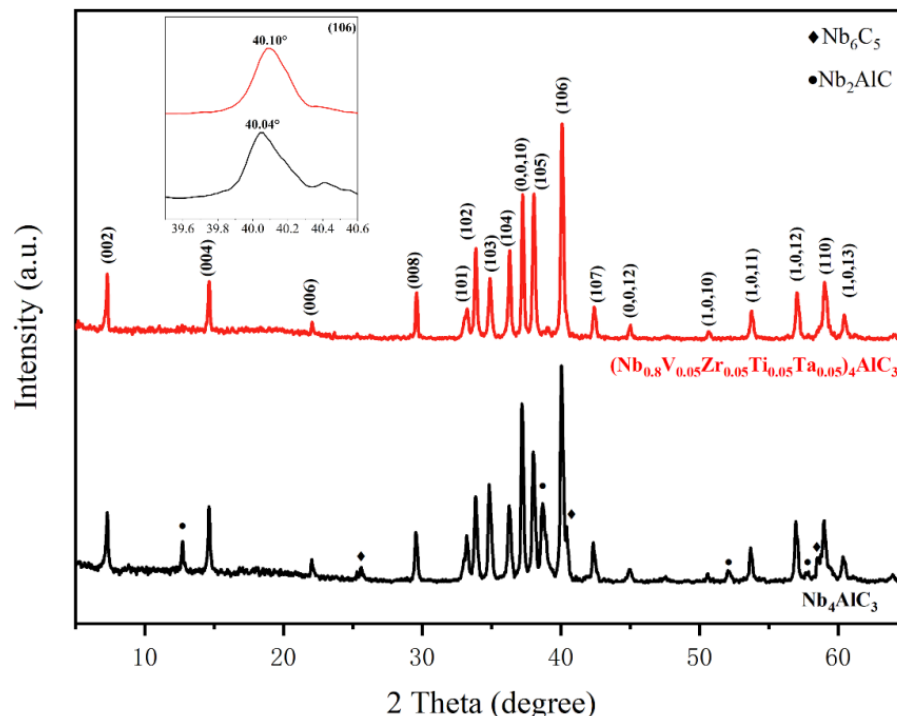**Figure 1.** X–ray diffraction (XRD) patterns of $(Nb_{0.8}Ti_{0.05}V_{0.05}Zr_{0.05}Ta_{0.05})_4AlC_3$ and Nb_4AlC_3 ceramics synthesized by spark plasma sintering.
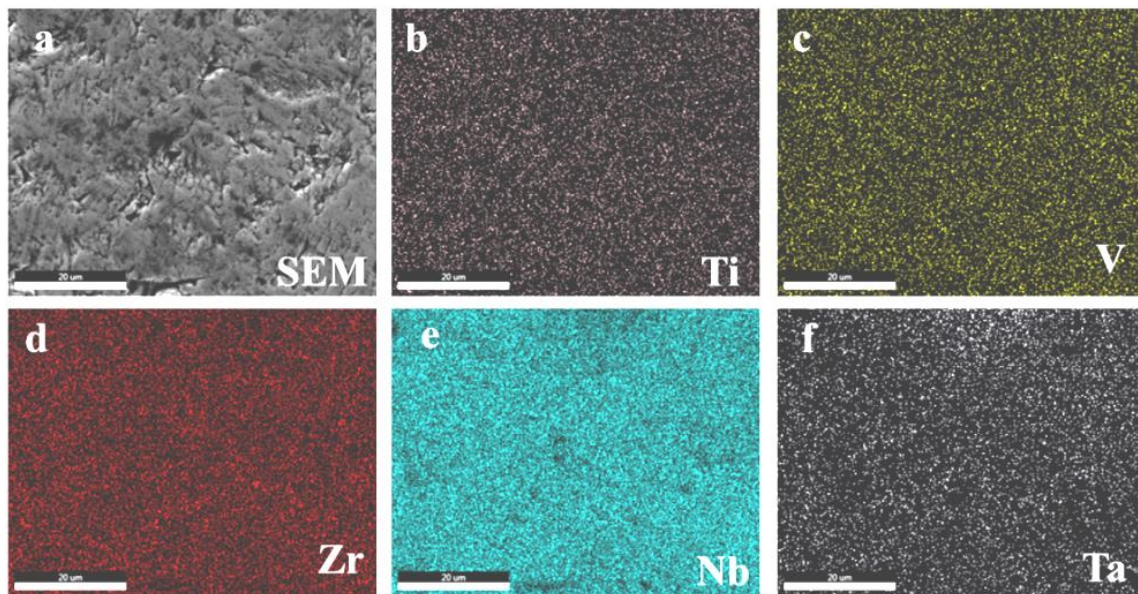
Figure 2. (**a**) Scanning electron microscopy (SEM) image of polished surface of $(Nb_{0.8}Ti_{0.05}V_{0.05}Zr_{0.05}Ta_{0.05})_4AlC_3$ ceramic; (**b**–**f**) element distribution of Ti, V, Zr, Nb, Ta examined by energy–dispersive spectroscopy (EDS).

When etching the LE–MAX $(Nb_{0.8}Ti_{0.05}V_{0.05}Zr_{0.05}Ta_{0.05})_4AlC_3$ powder with HF acid, different etching times and etching temperatures to get the optimal parameters were tried. The XRD results of the samples treated with different etching parameters are shown in Figure 3a. It is found that the etching effect of the LE–MAX $(Nb_{0.8}Ti_{0.05}V_{0.05}Zr_{0.05}Ta_{0.05})_4AlC_3$ powder for a long time of 120 h at room temperature is not obvious (green curve in Figure 3a). Although a broad characteristic XRD peak of MXene $(Nb_{0.8}Ti_{0.05}V_{0.05}Zr_{0.05}Ta_{0.05})_4C_3T_x$ is observed at low angles [1], its intensity is too low, and there is no significant change in the characteristic XRD peaks of the LE–MAX phase. This implies that long–time etching at room temperature could etch LE–MAX, but the etching efficiency was very low.

Since increasing the etching temperature could promote the etching reaction process [24,25], the etching effect was significantly improved by increasing the etching temperature to 50 °C and 60 °C, respectively, named 60–24 h–LE, 60–48 h–LE, and 50–48 h–LE samples. The sample name indicates its etching temperature, etching time, and sample type. For example, 60–48 h–LE means that the sample is a low–entropy $(Nb_{0.8}Ti_{0.05}V_{0.05}Zr_{0.05}Ta_{0.05})_4C_3T_x$ MXene etched at 60 °C for 48 h. It is observed that this sample has the characteristic (002) diffraction peak of MXene. The reason lies in that after the Al layer atoms in the $(Nb_{0.8}Ti_{0.05}V_{0.05}Zr_{0.05}Ta_{0.05})_4AlC_3$ phase were selectively etched, groups such as –OH and –F in the etching environment were inserted between the $(Nb_{0.8}Ti_{0.05}V_{0.05}Zr_{0.05}Ta_{0.05})_4C_3$ layers, and the nanosheets were obtained [26]. This makes the interlayer spacing of the $(Nb_{0.8}Ti_{0.05}V_{0.05}Zr_{0.05}Ta_{0.05})_4C_3T_x$ sheets change to be larger, resulting in a decrease in the intensity of the diffraction peak and an increase in the width [1,27,28]. In the XRD patterns of the 60–24 h–LE and 50–48 h–LE samples, many diffraction peaks of the residual $(Nb_{0.8}Ti_{0.05}V_{0.05}Zr_{0.05}Ta_{0.05})_4AlC_3$ phase can be clearly distinguished, which indicates that the LE–MAX phase was not completely etched under these two etching conditions of 60 °C–24 h and 50 °C–48 h. Therefore, the obtained 60–48 h–LE sample is the best LE–MXene $(Nb_{0.8}Ti_{0.05}V_{0.05}Zr_{0.05}Ta_{0.05})_4C_3T_x$.

Figure 3. (**a**) XRD patterns of LE–MXene $(Nb_{0.8}Ti_{0.05}V_{0.05}Zr_{0.05}Ta_{0.05})_4C_3T_x$ treated with different etching conditions; (**b**) XRD patterns of $Nb_4C_3T_x$ treated with different etching conditions.

To compare the effect of entropy enhancement on the etching effect, the etching test was carried out on Nb_4AlC_3 powder at 60 °C. Figure 3b shows the XRD patterns of $Nb_4C_3T_x$ samples obtained at different etching times. In the XRD pattern of sample 60–48 h (black curve in Figure 3b), the main diffraction peaks of the Nb_4AlC_3 phase have disappeared, and the characteristic peaks of $Nb_4C_3T_x$ MXene were also not observed. The diffraction peaks of Nb_6C_5 were observed, including the (200) peak at $2\theta = 34.9127°$, (131) peak at $2\theta = 40.5328°$, and $(\bar{1}33)$ peak at $2\theta = 58.6644°$. It might be considered that the etching time of 48 h at 60 °C was too serious for Nb_4AlC_3. At a high temperature, the loss of M–site elements increases with the increment of etching time, leading to the formation of the by–product Nb_6C_5. In the XRD pattern of the 60–12 h sample (red curve in Figure 3b), the peaks of the Nb_4AlC_3 phase almost disappeared, and the characteristic peaks of $Nb_4C_3T_x$ MXene were obvious. Same as in the LE–MXene $(Nb_{0.8}Ti_{0.05}V_{0.05}Zr_{0.05}Ta_{0.05})_4C_3T_x$ sample, there was an unavoidable peak of the by–product Nb_6C_5.

Figure 4a–d show the SEM images of etched 60–48 h–LE and 60–12 h samples at different magnifications. The lamellar structure can be clearly seen, and the obtained MXene is essentially multilayered. The results based on the EDS testing of the samples are summarized in Table 1. The atomic ratio of Al:M elements in the 60–48 h–LE sample decreased from 0.844:4.00 before etching to 0.034:4.00 after etching, and the atom ratio of the low–entropy Nb–based $(Nb_{0.8}Ti_{0.05}V_{0.05}Zr_{0.05}Ta_{0.05})_4C_3T_x$ is close to Nb:Ti:V:Zr:Ta = 0.8:0.04:0.05:0.05:0.05. It is proved that the Al elements in the precursor

$(Nb_{0.8}Ti_{0.05}V_{0.05}Zr_{0.05}Ta_{0.05})_4AlC_3$ and Nb_4AlC_3 phases have been essentially selectively etched, which is consistent with changes in the XRD patterns before and after etching. Additionally, the atomic ratio of Al:M elements in the 60–12 h sample decreased from 1.061:4.00 before etching to 0.095:4.00 after etching. It is proved that the Al atomic layers have been efficiently etched out.
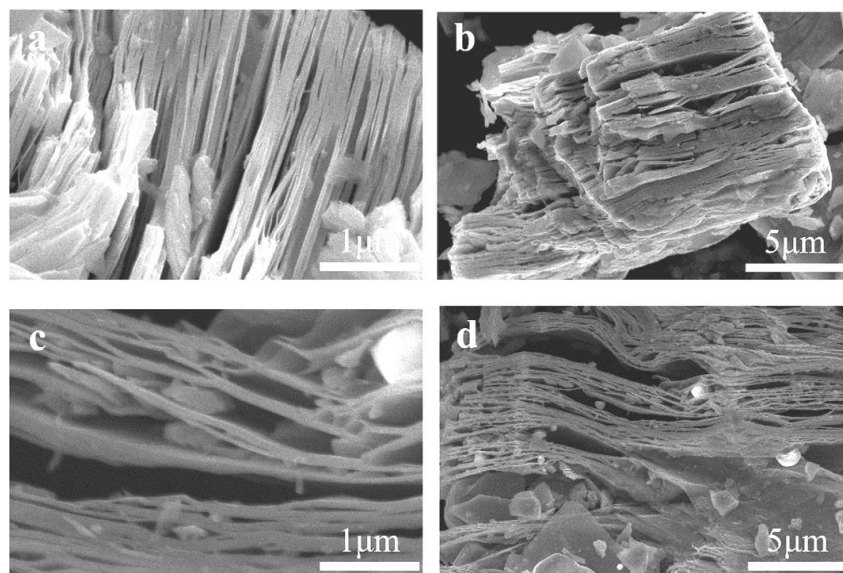

Figure 4. (**a**,**b**) SEM images of 60–48 h–LE $((Nb_{0.8}Ti_{0.05}V_{0.05}Zr_{0.05}Ta_{0.05})_4C_3T_x)$ MXene; (**c**,**d**) SEM images of 60–12 h $(Nb_4C_3T_x)$ MXene.

Table 1. Energy–dispersive spectroscopy (EDS) results of $(Nb_{0.8}Ti_{0.05}V_{0.05}Zr_{0.05}Ta_{0.05})_4AlC_3$ and Nb_4AlC_3 samples before and after etching.

Sample	Nb:Ti:V:Zr:Ta (Atomic Ratio)	Al: M–Site Elements (Atomic Ratio)
$(Nb_{0.8}Ti_{0.05}V_{0.05}Zr_{0.05}Ta_{0.05})_4AlC_3$	80:4.02:4.88:5.03:4.72	0.844:4.00
60–48 h–LE	80:5.81:6.52:2.58:7.64	0.034:4.00
Nb_4AlC_3	-	1.061:4.00
60–12 h	-	0.095:4.00

Based on the above results, it is concluded that the preparation of Nb_4C_3Tx requires less time than that of LE–MXene $(Nb_{0.8}Ti_{0.05}V_{0.05}Zr_{0.05}Ta_{0.05})_4C_3T_x$. In other words, the Al atomic layers of Nb_4AlC_3 are easier to etch selectively. This might be related to the M–site solid solution elements in the LE–MXene $(Nb_{0.8}Ti_{0.05}V_{0.05}Zr_{0.05}Ta_{0.05})_4C_3T_x$. It is speculated that the M–Al bond of $(Nb_{0.8}Ti_{0.05}V_{0.05}Zr_{0.05}Ta_{0.05})_4AlC_3$ is more energetic than the Nb–Al bond of Nb_4AlC_3, making a selective etching of the Al atomic layer more difficult [17,24,29]. The addition of M–site solid solution elements leads to the formation of lattice distortion and defects. As an electrode material, the lattice distortion and defects not only increase the resistance of ion diffusion but also change the conductivity of MXene, thus affecting the electrochemical performance. Therefore, the 60–48 h–LE and 60–12 h samples were used as electrode materials to assemble lithium–ion batteries for electrochemical testing.

Figure 5a,b show the obtained current–voltage (CV) curves of a lithium battery assembled by using the 60–48 h–LE and 60–12 samples, respectively, over a voltage range of 0.01 to 3 V (for Li/Li$^+$) with a scan rate of 1 mV/s. For the 60–48 h–LE sample, in the first scan cycle, an obvious reduction peak was observed at 1.20 V, and a less obvious reduction peak was observed at 0.25 V. These two reduction peaks were no longer observed in the subsequent scan cycles, and the reactions that occurred were irreversible chemical processes of solid electrolyte interface (SEI) film formation and Li$^+$ insertion into the

$(Nb_{0.8}Ti_{0.05}V_{0.05}Zr_{0.05}Ta_{0.05})_4C_3T_x$ sheets [30–32]. The oxidation peaks at 0.40 V and 1.65 V correspond to the chemical process of Li^+ deintercalation in the active material. After the first scan cycle, the 1.65 V oxidation peak decreased and then gradually stabilized. The oxidation peak at 0.40 V was observed and stabilized in the second scan cycle. It indicates that the Li^+ deintercalation behavior was gradually stable after the first cycle [33]. The reason is that due to the existence of lattice distortion and lattice defects, the ion diffusion resistance of LE–MXene $(Nb_{0.8}Ti_{0.05}V_{0.05}Zr_{0.05}Ta_{0.05})_4C_3T_x$ increases. Because the battery energy storage behavior depends on the redox reactions, and the larger ion diffusion resistance prevents the redox reactions from proceeding smoothly, this results in a decrease in the proportion of battery behavior in the energy storage behavior of $(Nb_{0.8}Ti_{0.05}V_{0.05}Zr_{0.05}Ta_{0.05})_4C_3T_x$, and there are no obvious redox peaks on the CV curve. Overall, the CV curve of the 60–48 h–LE sample shows a rectangular–like curve profile with no obvious oxidation peaks, except for the first scan cycle. It can be inferred that its energy storage behavior is mainly pseudo-capacitive behavior [34] and some battery behavior [35,36]. For the 60–12 h sample, the shape of the CV curve for the first scan cycle is almost identical to that of the previously discussed CV curve for LE–MXene $(Nb_{0.8}Ti_{0.05}V_{0.05}Zr_{0.05}Ta_{0.05})_4C_3T_x$. However, from the second scan cycle onward, the CV curve is very different from the former. After the second scan cycle, a stable reduction peak was observed at about 1.75 V and 2.20 V, while a stable oxidation peak was observed at about 2.50 V. The battery behavior is proved to be a greater contributor to its energy storage behavior than the former.
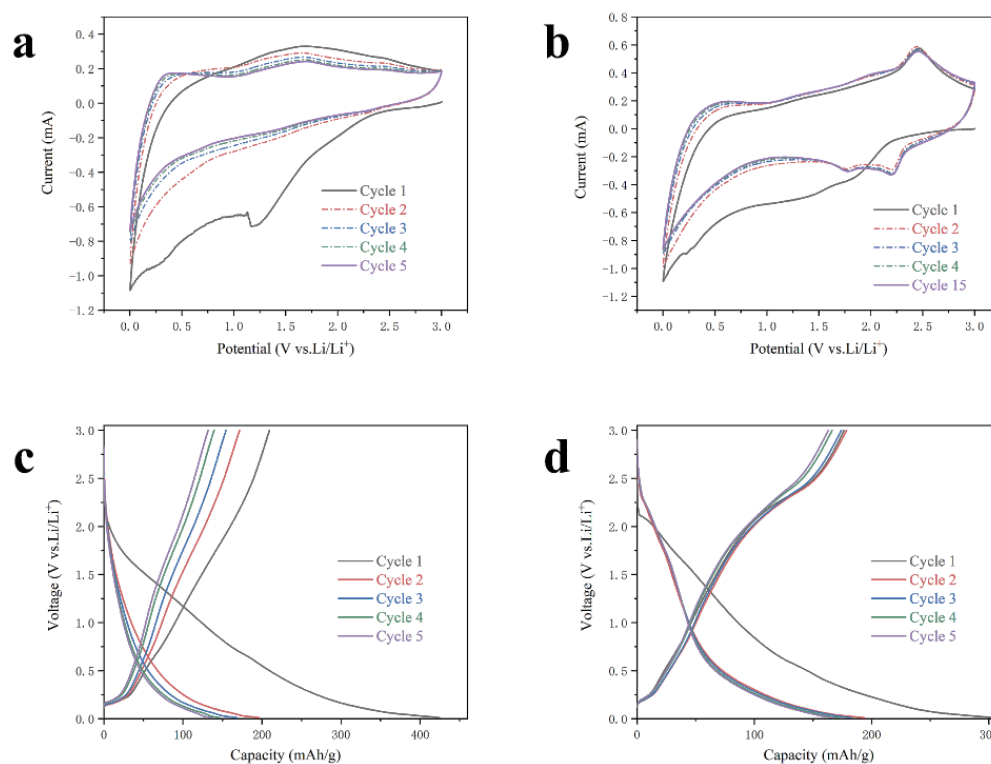

Figure 5. Current–voltage (CV) curves of lithium batteries assembled by using (**a**) 60–48 h–LE ($(Nb_{0.8}Ti_{0.05}V_{0.05}Zr_{0.05}Ta_{0.05})_4C_3T_x$) and (**b**) 60–12 h ($Nb_4C_3T_x$) samples, and galvanostatic charge–discharge curves of lithium batteries assembled by using (**c**) 60–48 h–LE ($(Nb_{0.8}Ti_{0.05}V_{0.05}Zr_{0.05}Ta_{0.05})_4C_3T_x$) and (**d**) 60–12 h ($Nb_4C_3T_x$) samples.

Figure 5c,d show the galvanostatic charge–discharge curve of a lithium battery assembled by using the 60–48 h–LE and 60–12 samples at a current density of 0.1 A·g^{-1} and a voltage range of 0.01~3 V. The first charge/discharge capacities (initial coulombic efficiency) of the 60–48 h–LE and 60–12 h samples are 209.3/424.9(49.28%) and 176.6/304.7(57.95%) mAh·g^{-1}, respectively. Both samples have a large irreversible capacity, which is related

to the formation of SEI and the unsuccessful deinsertion of Li^+ after partial embedding in the active material sheet structure [37]. However, after several cycles, the reversible capacity gradually stabilized, and finally, the coulombic efficiency stabilized close to 100%, indicating that the batteries had good stability. After cycling stability, the reversible specific capacities of the lithium battery assembled by using the 60–48 h–LE and 60–12 h samples are about 135 and 160 mAh·g^{-1}, respectively. In addition, the lithium battery assembled by using the 60–12 h sample entered the steady state relatively quickly and was almost stable in the second cycle. The following electrostatic charge–discharge curves almost coincided with the second cycle onward. This might be related to the full separation of the sample layer during the etching process, which contributes to the insertion and removal of Li+ during the charge–discharge cycle rapidly going into a steady state. Due to the lattice distortion and defects caused by the existence of solid solution elements in the LE–MXene $(Nb_{0.8}Ti_{0.05}V_{0.05}Zr_{0.05}Ta_{0.05})_4C_3T_x$, during the charge–discharge process, the layer spacing may change continuously with the repeated insertion and exit of Li^+, stabilizing after a few cycles. Meanwhile, the $Nb_4C_3T_x$ has only Nb at the M–site, so there is no such process, and they enter a steady state after one charge–discharge cycle. The galvanostatic charge–discharge curves of the two lithium batteries have no obvious platform and show an inclined linear shape. In addition, the galvanostatic charge–discharge curve shows clear changes in slope at the voltage position where the redox peak of the CV curve appears. Such galvanostatic charge–discharge curves show that the energy storage mechanism of $(Nb_{0.8}Ti_{0.05}V_{0.05}Zr_{0.05}Ta_{0.05})_4C_3T_x$ and $Nb_4C_3T_x$ is a mixture of pseudocapacitive behavior and battery behavior. Therefore, the present result is consistent with the previous analysis of the CV curves.

Figure 6a,c show the cycle performance curves of lithium batteries assembled by using the 60–48 h–LE and 60–12 h samples, respectively. The measured specific discharge capacities of two kinds of batteries were 130.0 mAh·g^{-1} and 163.7 mAh·g^{-1}, respectively, after 50 charge–discharge cycles at the current density of 0.1 A·g^{-1}. Three different current densities of 0.1, 0.2, and 0.5 A·g^{-1} were used in the rate performance tests. Figure 6b,d show the rate performance curves of lithium batteries assembled by using the 60–48 h–LE and 60–12 h samples, respectively. The tested specific capacities of the lithium batteries containing 60–48 h–LE $((Nb_{0.8}Ti_{0.05}V_{0.05}Zr_{0.05}Ta_{0.05})_4C_3T_x)$ MXene were 123.1, 68.7, and 35.2 mAh·g^{-1} at the current densities of 0.1, 0.2, and 0.5 A·g^{-1}, respectively. When the current density was restored to 0.1 A·g^{-1}, the specific capacity recovered to 112.6 mAh·g^{-1}. Additionally, it is seen that the measured specific capacities of the lithium battery containing the 60–12 h $(Nb_4C_3T_x)$ sample were 164.7, 116.1, and 72.2 mAh·g^{-1} at the current densities of 0.1, 0.2, and 0.5 A·g^{-1}, respectively. When the current density was decreased to 0.1 A·g^{-1}, the specific capacity increased to 169.5 mAh·g^{-1} again. It is concluded that the electrochemical properties of the 60–12 h sample are better than those of the 60–48 h–LE sample, which is consistent with the results of some researchers who added a single solid solution element at the M–site [22]. For example, Yang et al. attempted to add a single solid solution element of 20 at.% to the M–site, resulting in the specific capacity losses of 16.4% (solid solution element Ti) and 30.2% (solid solution element Zr) [22]. They found that after 20 cycles at a rate of 0.25C (equivalent to a current density of 0.0395 A/g based on a specific capacity of 158 mAh/g), the batteries containing $(Nb_{0.8}Ti_{0.2})_4C_3T_x$ and $(Nb_{0.8}Zr_{0.2})_4C_3T_x$ still had the specific capacities of 158 and 132 mAh/g, respectively. Comparatively, the present prepared lithium battery containing $(Nb_{0.8}Ti_{0.05}V_{0.05}Zr_{0.05}Ta_{0.05})_4C_3T_x$ still had a specific capacity of 163.7 mAh/g after 50 cycles at a current density of 0.1 A/g. Therefore, this work achieved a larger specific capacity at a higher current density.

The specific capacitance loss of a lithium battery containing the 60–48 h–LE sample was 20.6% compared to that containing the 60–12 h sample. It seems that increasing the entropy of MXene by increasing the type of M–site elements in the low–entropy range could not improve the energy storage performance of MXene. It is speculated that the possible reasons for the lower discharge–specific capacity of the lithium battery containing the 60–48 h–LE sample are as follows: Firstly, it is more difficult to etch $(Nb_{0.8}Ti_{0.05}V_{0.05}Zr_{0.05}Ta_{0.05})_4AlC_3$

after entropy increase treatment. Longer etching time (48 h) and high etching temperature (60 °C) bring by–product Nb_6C_5, which has a negative effect on lithium storage. Secondly, the lattice distortion and defects caused by entropy increase treatment change the electrical conductivity of MXene and hinder the diffusion of ions in MXene.
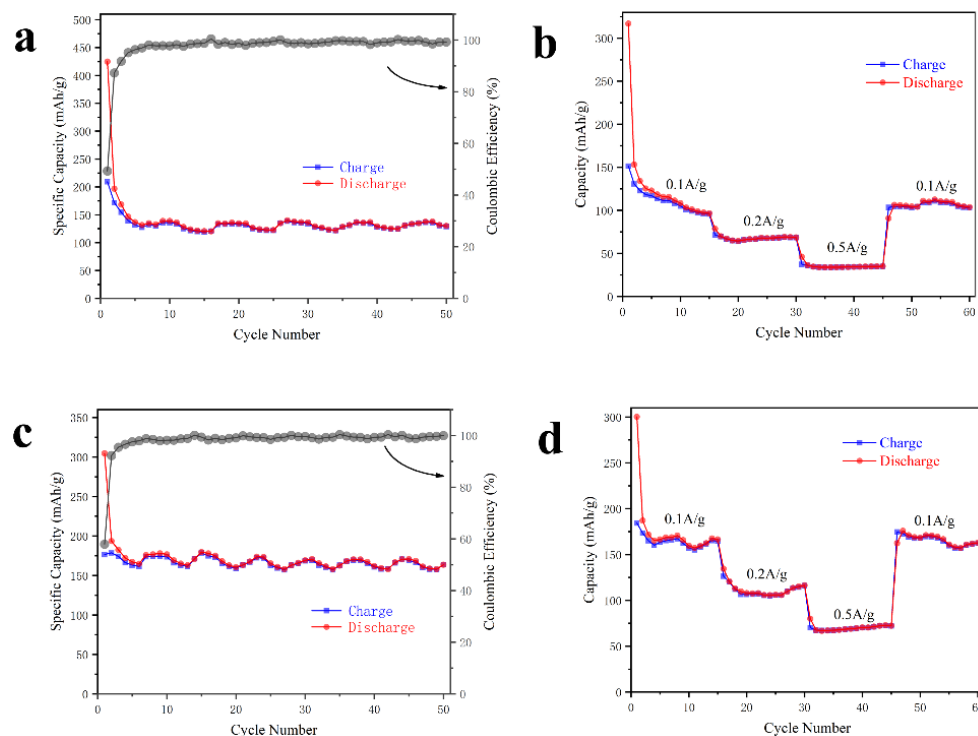

Figure 6. Cyclic performance curves and rate performance curves of lithium batteries assembled by using the (**a**,**b**) 60–48 h–LE (($Nb_{0.8}Ti_{0.05}V_{0.05}Zr_{0.05}Ta_{0.05})_4C_3T_x$) and (**c**,**d**) 60–12 h ($Nb_4C_3T_x$) samples.

Figure 7 shows the electrochemical impedance spectra (EIS) curves of lithium batteries assembled by using the 60–48 h–LE and 60–12 h samples. The intersection of the high–frequency semicircle and the *x*–axis corresponds to the intrinsic resistance (R_s) of the battery. The radius of the high–frequency semicircle corresponds to the charge transfer impedance (R_{ct}) in the battery system. The slope of the low–frequency line represents the diffusion impedance (W). The larger the slope, the greater the ion diffusion coefficient [31,38]. The intrinsic resistance of both kinds of batteries is low due to the high electrical conductivities of ($Nb_{0.8}Ti_{0.05}V_{0.05}Zr_{0.05}Ta_{0.05})_4C_3T_x$ and $Nb_4C_3T_x$ MXene. Here, the intrinsic resistance of a lithium battery containing ($Nb_{0.8}Ti_{0.05}V_{0.05}Zr_{0.05}Ta_{0.05})_4C_3T_x$ is larger, which corresponds to the result that the lattice distortion and lattice defects caused by entropy enhancement reduce the electrical conductivity of ($Nb_{0.8}Ti_{0.05}V_{0.05}Zr_{0.05}Ta_{0.05})_4C_3T_x$. Also, the lattice distortion in the LE–MXene ($Nb_{0.8}Ti_{0.05}V_{0.05}Zr_{0.05}Ta_{0.05})_4C_3T_x$ increases the ion diffusion resistance, which hinders the redox reaction in the energy storage process. Reversely, the ion diffusion resistance of a lithium battery containing $Nb_4C_3T_x$ is significantly lower than that containing ($Nb_{0.8}Ti_{0.05}V_{0.05}Zr_{0.05}Ta_{0.05})_4C_3T_x$, which is related to fewer defects in $Nb_4C_3T_x$. So, the lithium battery containing the 60–12 h ($Nb_4C_3T_x$) sample has a proportionally higher energy storage capacity than that containing the 60–48 h–LE (($Nb_{0.8}Ti_{0.05}V_{0.05}Zr_{0.05}Ta_{0.05})_4C_3T_x$) sample.

In addition, the amount of by–products was well controlled in the 60–48 h–LE (($Nb_{0.8}Ti_{0.05}V_{0.05}Zr_{0.05}Ta_{0.05})_4C_3T_x$) and 60–12 h ($Nb_4C_3T_x$) samples prepared by appropriate etching conditions. Therefore, the influence of by–products on the electrochemical performance is limited, and the assembled lithium batteries show good energy storage capability. For the field of energy storage, as long as the etching conditions are properly controlled, the effect of by–products is acceptable, and it is feasible to increase the tempera-

ture to improve the etching efficiency. This attempt is also of informative interest in other applications. The present study reveals the importance of MXene nanosheets in promising applications in the functional energy storage fields [39–41].
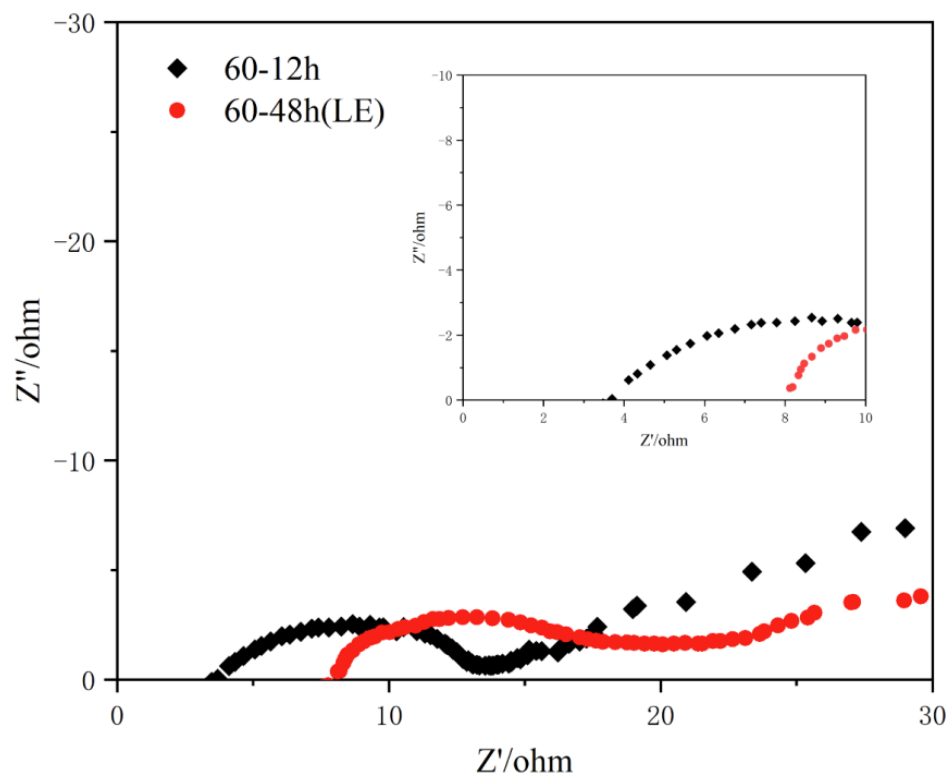

Figure 7. Electrochemical impedance spectra (EIS) curves of lithium batteries assembled by using the 60–48 h–LE (($Nb_{0.8}Ti_{0.05}V_{0.05}Zr_{0.05}Ta_{0.05})_4C_3T_x$) and 60–12 h ($Nb_4C_3T_x$) samples.

4. Conclusions

In this work, $Nb_4C_3T_x$ and $(Nb_{0.8}Ti_{0.05}V_{0.05}Zr_{0.05}Ta_{0.05})_4C_3T_x$ MXenes were successfully prepared by etching Nb_4AlC_3 and $(Nb_{0.8}Ti_{0.05}V_{0.05}Zr_{0.05}Ta_{0.05})_4AlC_3$ at 60 °C in the HF acid. The energy storage capacity of lithium batteries containing $Nb_4C_3T_x$ and $(Nb_{0.8}Ti_{0.05}V_{0.05}Zr_{0.05}Ta_{0.05})_4C_3T_x$ MXenes were systematically investigated, and the achieved results are listed as follows:

(1) As the electrode material of a lithium–ion battery, the resulting $Nb_4C_3T_x$ MXene provided the reversible capacity of 163.7 mAh·g^{-1} after 50 cycles at 0.1 A·g^{-1}, maintaining the coulombic efficiency close to 100%. The measured specific capacities of the lithium batteries containing $Nb_4C_3T_x$ MXene were 164.7, 116.1, and 72.2 mAh·g^{-1} at the current densities of 0.1, 0.2, and 0.5 A·g^{-1}, respectively. When the current density was decreased to 0.1 A·g^{-1}, the specific capacity increased to 169.5 mAh·g^{-1} again.

(2) The lithium battery containing LE–MXene $(Nb_{0.8}Ti_{0.05}V_{0.05}Zr_{0.05}Ta_{0.05})_4C_3T_x$ exhibited the reversible capacity of 130 mAh·g^{-1} at 0.1 A·g^{-1} after 50 cycles. Also, the coulombic efficiency retained the high value close to 100%. The tested specific capacities of the lithium batteries containing $(Nb_{0.8}Ti_{0.05}V_{0.05}Zr_{0.05}Ta_{0.05})_4C_3T_x$ MXene were 123.1, 68.7, and 35.2 mAh·g^{-1} at the current densities of 0.1, 0.2, and 0.5 A·g^{-1}, respectively. When the current density was restored to 0.1 A·g^{-1}, the specific capacity recovered to 112.6 mAh·g^{-1}.

(3) It is concluded that the specific capacity of a lithium battery containing $Nb_4C_3T_x$ MXene was higher than that of a lithium battery containing LE–MXene ($Nb_{0.8}Ti_{0.05}V_{0.05}$ $Zr_{0.05}Ta_{0.05})_4C_3T_x$ MXene, which was ascribed to the existence of lattice distortion and

defects in the LE–MXene which hindered the diffusion of lithium ions and reduced the reversible insertion and extraction of lithium ions.

(4) The present work proved the promising applications of $Nb_4C_3T_x$ and $(Nb_{0.8}Ti_{0.05}V_{0.05}Zr_{0.05}Ta_{0.05})_4C_3T_x$ MXenes in lithium batteries.

Author Contributions: Conceptualization, C.H.; methodology, H.C., L.C. and Q.F.; software, M.F.; formal analysis, H.C., L.C. and Q.F.; investigation, M.F.; resources, J.C.; data curation, J.C.; writing—original draft preparation, H.C.; writing—review and editing, M.F., J.C., L.C., Q.F. and C.H.; visualization, H.C.; supervision, L.C., Q.F. and C.H.; project administration, C.H.; funding acquisition, M.F. All authors have read and agreed to the published version of the manuscript.

Data Availability Statement: The data presented in this study are available on request from the corresponding author. The data are not publicly available due to all the dataset created during this research belong to the funder according to the contract.

Conflicts of Interest: The authors declare no conflict of interest.

References

1. Naguib, M.; Kurtoglu, M.; Presser, V.; Lu, J.; Niu, J.; Heon, M.; Hultman, L.; Gogotsi, Y.; Barsoum, M.W. Two-dimensional nanocrystals produced by exfoliation of Ti_3AlC_2. *Adv. Mater.* **2011**, *23*, 4248–4253. [CrossRef]
2. Ghidiu, M.; Lukatskaya, M.R.; Zhao, M.-Q.; Gogotsi, Y.; Barsoum, M.W. Conductive two-dimensional titanium carbide 'clay' with high volumetric capacitance. *Nature* **2014**, *516*, 78–81. [CrossRef]
3. Naguib, M.; Mashtalir, O.; Carle, J.; Presser, V.; Lu, J.; Hultman, L.; Gogotsi, Y.; Barsoum, M.W. Two-dimensional transition metal carbides. *Acs Nano* **2012**, *6*, 1322–1331. [CrossRef]
4. Zhang, X.; Zhang, Z.; Zhou, Z. MXene-based materials for electrochemical energy storage. *J. Energy Chem.* **2018**, *27*, 73–85. [CrossRef]
5. Naguib, M.; Come, J.; Dyatkin, B.; Presser, V.; Taberna, P.-L.; Simon, P.; Barsoum, M.W.; Gogotsi, Y. MXene: A promising transition metal carbide anode for lithium-ion batteries. *Electrochem. Commun.* **2012**, *16*, 61–64. [CrossRef]
6. Kim, S.J.; Naguib, M.; Zhao, M.; Zhang, C.; Jung, H.-T.; Barsoum, M.W.; Gogotsi, Y. High mass loading, binder-free MXene anodes for high areal capacity Li-ion batteries. *Electrochim. Acta* **2015**, *163*, 246–251. [CrossRef]
7. Lukatskaya, M.R.; Mashtalir, O.; Ren, C.E.; Dall'Agnese, Y.; Rozier, P.; Taberna, P.L.; Naguib, M.; Simon, P.; Barsoum, M.W.; Gogotsi, Y. Cation intercalation and high volumetric capacitance of two-dimensional titanium carbide. *Science* **2013**, *341*, 1502–1505. [CrossRef]
8. Li, X.; Fan, G.; Zeng, C. Synthesis of ruthenium nanoparticles deposited on graphene-like transition metal carbide as an effective catalyst for the hydrolysis of sodium borohydride. *Int. J. Hydrogen Energy* **2014**, *39*, 14927–14934. [CrossRef]
9. Gao, Y.; Wang, L.; Li, Z.; Zhou, A.; Hu, Q.; Cao, X. Preparation of MXene-Cu_2O nanocomposite and effect on thermal decomposition of ammonium perchlorate. *Solid State Sci.* **2014**, *35*, 62–65. [CrossRef]
10. Peng, Q.; Guo, J.; Zhang, Q.; Xiang, J.; Liu, B.; Zhou, A.; Liu, R.; Tian, Y. Unique lead adsorption behavior of activated hydroxyl group in two-dimensional titanium carbide. *J. Am. Chem. Soc.* **2014**, *136*, 4113–4116. [CrossRef]
11. Hu, Q.; Sun, D.; Wu, Q.; Wang, H.; Wang, L.; Liu, B.; Zhou, A.; He, J. MXene: A new family of promising hydrogen storage medium. *J. Phys. Chem. A* **2013**, *117*, 14253–14260. [CrossRef]
12. Lin, H.; Wang, Y.; Gao, S.; Chen, Y.; Shi, J. Theranostic 2D tantalum carbide (MXene). *Adv. Mater.* **2018**, *30*, 1703284. [CrossRef]
13. Yeh, J.W.; Chen, S.K.; Lin, S.J.; Gan, J.Y.; Chin, T.S.; Shun, T.T.; Tsau, C.H.; Chang, S.Y. Nanostructured high-entropy alloys with multiple principal elements: Novel alloy design concepts and outcomes. *Adv. Eng. Mater.* **2004**, *6*, 299–303. [CrossRef]
14. Cantor, B.; Chang, I.T.H.; Knight, P.; Vincent, A.J.B. Microstructural development in equiatomic multicomponent alloys. *Mater. Sci. Eng. A-Struct. Mater. Prop. Microstruct. Process.* **2004**, *375*, 213–218. [CrossRef]
15. Yeh, J.-W. Recent progress in high-entropy alloys. *Ann. Chim. Sci. Mater.* **2006**, *31*, 633–648. [CrossRef]
16. Rost, C.M.; Sachet, E.; Borman, T.; Moballegh, A.; Dickey, E.C.; Hou, D.; Jones, J.L.; Curtarolo, S.; Maria, J.-P. Entropy-stabilized oxides. *Nat. Commun.* **2015**, *6*, 8485. [CrossRef]
17. Du, Z.; Wu, C.; Chen, Y.; Cao, Z.; Hu, R.; Zhang, Y.; Gu, J.; Cui, Y.; Chen, H.; Shi, Y.; et al. High-entropy atomic layers of transition-metal carbides (MXenes). *Adv. Mater.* **2021**, *33*, 2101473. [CrossRef]
18. Etman, A.S.; Zhou, J.; Rosen, J. $Ti_{1.1}V_{0.7}Cr_xNb_{1.0}Ta_{0.6}C_3T_z$ high-entropy MXene freestanding films for charge storage applications. *Electrochem. Commun.* **2022**, *137*, 107264. [CrossRef]
19. Du, Z.; Wu, C.; Chen, Y.; Zhu, Q.; Cui, Y.; Wang, H.; Zhang, Y.; Chen, X.; Shang, J.; Li, B.; et al. High-entropy carbonitride MAX phases and their derivative MXenes. *Adv. Energy Mater.* **2022**, *12*, 2103228. [CrossRef]
20. Ma, W.; Wang, M.; Yi, Q.; Huang, D.; Dang, J.; Lv, Z.; Lv, X.; Zhang, S. A new $Ti_2V_{0.9}Cr_{0.1}C_2T_x$ MXene with ultrahigh gravimetric capacitance. *Nano Energy* **2022**, *96*, 107129. [CrossRef]

21. Zhou, J.; Tao, Q.; Ahmed, B.; Palisaitis, J.; Persson, I.; Halim, J.; Barsoum, M.W.; Persson, P.O.A.; Rosen, J. High-entropy laminate metal carbide (MAX phase) and its two-dimensional derivative MXene. *Chem. Mater.* **2022**, *34*, 2098–2106. [CrossRef]

22. Yang, J.; Naguib, M.; Ghidiu, M.; Pan, L.-M.; Gu, J.; Nanda, J.; Halim, J.; Gogotsi, Y.; Barsoum, M.W. Two-dimensional Nb-based M_4C_3 solid solutions (MXenes). *J. Am. Ceram. Soc.* **2016**, *99*, 660–666. [CrossRef]

23. Cai, P.; He, Q.; Wang, L.; Liu, X.; Yin, J.; Liu, Y.; Huang, Y.; Huang, Z. Two-dimensional Nb-based M_4C_3Tx MXenes and their sodium storage performances. *Ceram. Int.* **2019**, *45*, 5761–5767. [CrossRef]

24. Naguib, M.; Mochalin, V.N.; Barsoum, M.W.; Gogotsi, Y. 25th anniversary article: MXenes: A new family of two-dimensional materials. *Adv. Mater.* **2014**, *26*, 992–1005. [CrossRef]

25. Mashtalir, O.; Naguib, M.; Dyatkin, B.; Gogotsi, Y.; Barsoum, M.W. Kinetics of aluminum extraction from Ti_3AlC_2 in hydrofluoric acid. *Mater. Chem. Phys.* **2013**, *139*, 147–152. [CrossRef]

26. Naguib, M.; Halim, J.; Lu, J.; Cook, K.M.; Hultman, L.; Gogotsi, Y.; Barsoum, M.W. New two-dimensional niobium and vanadium carbides as promising materials for Li-ion batteries. *J. Am. Chem. Soc.* **2013**, *135*, 15966–15969. [CrossRef]

27. Zhao, S.; Meng, X.; Zhu, K.; Du, F.; Chen, G.; Wei, Y.; Gogotsi, Y.; Gao, Y. Li-ion uptake and increase in interlayer spacing of Nb_4C_3 MXene. *Energy Storage Mater.* **2017**, *8*, 42–48. [CrossRef]

28. Ghidiu, M.; Naguib, M.; Shi, C.; Mashtalir, O.; Pan, L.M.; Zhang, B.; Yang, J.; Gogotsi, Y.; Billinge, S.J.L.; Barsoum, M.W. Synthesis and characterization of two-dimensional Nb_4C_3 (MXene). *Chem. Commun.* **2014**, *50*, 9517–9520. [CrossRef]

29. Lei, J.-C.; Zhang, X.; Zhou, Z. Recent advances in MXene: Preparation, properties, and applications. *Front. Phys.* **2015**, *10*, 276–286. [CrossRef]

30. Zhan, R.; Zhang, Y.; Chen, H.; Xu, Q.; Ma, Q.; Gao, W.; Yang, T.; Jiang, J.; Bao, S.; Xu, M. High-rate and long-life sodium-ion batteries based on sponge-like three-dimensional porous Na-rich ferric pyrophosphate cathode material. *Acs Appl. Mater. Interfaces* **2019**, *11*, 5107–5113. [CrossRef]

31. Hui, X.; Zhao, R.; Zhang, P.; Li, C.; Wang, C.; Yin, L. Low-temperature reduction strategy synthesized Si/Ti_3C_2 MXene composite anodes for high-performance Li-ion batteries. *Adv. Energy Mater.* **2019**, *9*, 1901065. [CrossRef]

32. Tao, M.; Du, G.; Zhang, Y.; Gao, W.; Liu, D.; Luo, Y.; Jiang, J.; Bao, S.; Xu, M. TiO_xN_y nanoparticles/C composites derived from MXene as anode material for potassium-ion batteries. *Chem. Eng. J.* **2019**, *369*, 828–833. [CrossRef]

33. Zou, G.; Zhang, Z.; Guo, J.; Liu, B.; Zhang, Q.; Fernandez, C.; Peng, Q. Synthesis of MXene/Ag composites for extraordinary long cycle lifetime lithium storage at high rates. *ACS Appl. Mater. Interfaces* **2016**, *8*, 22280–22286. [CrossRef] [PubMed]

34. Okubo, M.; Sugahara, A.; Kajiyama, S.; Yamada, A. MXene as a charge storage host. *Acc. Chem. Res.* **2018**, *51*, 591–599. [CrossRef] [PubMed]

35. Ko, J.S.; Sassin, M.B.; Rolison, D.R.; Long, J.W. Deconvolving double-layer, pseudocapacitance, and battery-like charge-storage mechanisms in nanoscale $LiMn_2O_4$ at 3D carbon architectures. *Electrochim. Acta* **2018**, *275*, 225–235. [CrossRef]

36. Jiang, Y.; Liu, J. Definitions of pseudocapacitive materials: A brief review. *Energy Environ. Mater.* **2019**, *2*, 30–37. [CrossRef]

37. Xie, Y.; Naguib, M.; Mochalin, V.N.; Barsoum, M.W.; Gogotsi, Y.; Yu, X.; Nam, K.-W.; Yang, X.-Q.; Kolesnikov, A.I.; Kent, P.R.C. Role of surface structure on Li-ion energy storage capacity of two-dimensional transition-metal carbides. *J. Am. Chem. Soc.* **2014**, *136*, 6385–6394. [CrossRef]

38. Xia, Z.; Chen, X.; Ci, H.; Fan, Z.; Yi, Y.; Yin, W.; Wei, N.; Cai, J.; Zhang, Y.; Sun, J. Designing N-doped graphene/$ReSe_2$/Ti_3C_2 MXene heterostructure frameworks as promising anodes for high-rate potassium-ion batteries. *J. Energy Chem.* **2021**, *53*, 155–162. [CrossRef]

39. Xiong, Y.; Shepherd, S.; Tibbs, J.; Bacon, A.; Liu, W.; Akin, L.D.; Ayupova, T.; Bhaskar, S.; Cunningham, B.T. Photonic crystal enhanced fluorescence: A review on design strategies and applications. *Micromachines* **2023**, *14*, 668. [CrossRef]

40. Bhaskar, S.; Kambhampati, N.S.V.; Ganesh, K.M.; Sharma, M.P.; Srinivasan, V.; Ramamurthy, S.S. Metal-free, graphene, oxide-based tunable soliton and plasmon engineering for biosensing applications. *ACS Appl. Mater. Interfaces* **2021**, *13*, 17046–17061. [CrossRef]

41. Yang, W.; Cai, X.; Guo, S.; Wen, L.; Sun, Z.; Shang, R.; Shi, X.; Wang, J.; Chen, H.; Li, Z. A high performance triboelectric nanogenerator based on MXene/Graphene oxide electrode for glucose detection. *Materials* **2023**, *16*, 841. [CrossRef] [PubMed]